Combustion Generated Fine Carbonaceous Particles

Proceedings of an International Workshop
held in Villa Orlandi, Anacapri,
May 13-16, 2007

edited by
H. Bockhorn
A. D'Anna
A. F. Sarofim
H. Wang

KIT Scientific Publishing

g a soot particle"
ppiavoce.it)

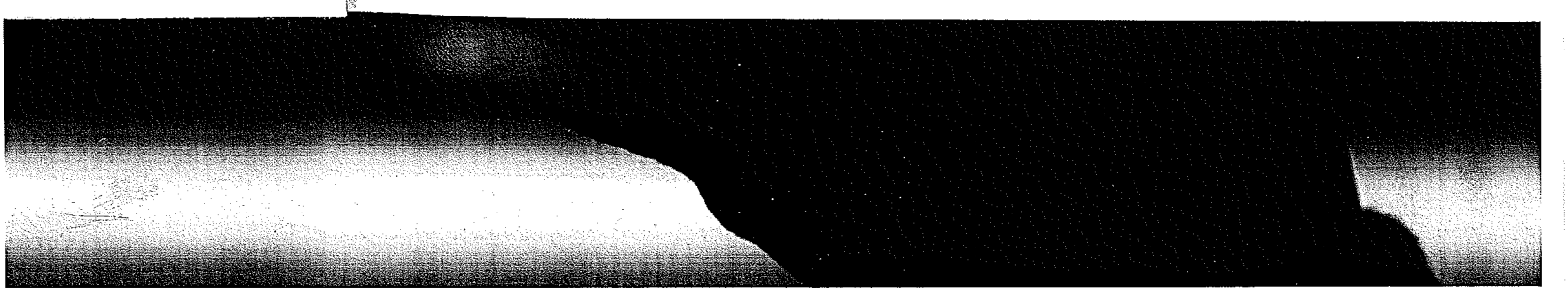

Chapter 33

Size resolved soot surface oxidation kinetics

A.A. Lall, M.R. Zachariah
Departments of Mechanical Engineering and Chemistry and Biochemistry
University of Maryland, College Park, MD 20742
Ph: 301-405-4311, Fax: 301-314-9477
Email: mrz@umd.edu

Abstract: In this paper we summarize a number of our soot surface-oxidation kinetics measurements. The measurement methods include: (a) direct visualization using electron microscopy and (d) tandem differential mobility analysis (TDMA). Arrhenious kinetic analysis allows us to extract the oxidation rate, and activation energies for flame, diesel and bio-diesel soot as well as the role of metals in soot oxidation.

For flame soot oxidation, a activation energy of 148 kJ/mol was found at low temperatures (< 800K). Using the TDMA method, the activation energy of soot oxidation in air was equal to 163 kJ·mol^{-1} over the temperature range 800°-1120° C. The reasons for the difference in activation energies at low and high temperatures are discussed. The activation energies were 114, 109, and 108 kJ mol^{-1} for the 10, 50, and 75% load diesel nanoparticles sampled directly from a medium duty diesel engine exhaust over the temperature range of 800 1140 °C. The reason for the low activation energies of diesel soot compared to that of flame soot is attributed to the presence of metals in the diesel fuel, possibly coming from lubricating oils. To test the influence of metals in soot oxidation, cerium was added to diesel fuel and iron was added to flame soot in two separate studies. It was found that the addition of iron to a flame reduced the activation energy significantly from ~162±3 kJ/mol to ~116±3 kJ/mol, comparable with diesel engine generated soot with an activation energy ~ 110 kJ/mol.

The oxidation kinetics for bio-diesel was found to be ~6 times higher than that of regular diesel fuel in the temperature range of 700 to 825 °C.

1. INTRODUCTION

Soot is produced by incomplete combustion or pyrolysis of hydrocarbon fuels and is a useful material termed "carbon black" which is widely used in printing inks, and in rubber and plastic products. The global market demands carbon black in millions of tons every year. On the other hand, soot is released into the atmosphere as an undesirable product by several natural and man-made combustion processes such as wood burning, diesel engine exhaust emissions [1], power plants, air craft emissions[2]. Soot is known to be harmful to the respiratory tract if inhaled, especially when the particles are less than 5 μm in diameter. Recently it has been revealed that carbon soot emission from combustion is an important factor leading to climate change [3, 4]. A typical transmission electron microscope (TEM) image of a soot aggregate is shown in Figure 1. The aggregate is composed of individual particles termed primary particles of about 30 nm in diameter.

Figure 1. A typical transmission electron microscope (TEM) image of an atmospheric aggregate is shown in Figure 1. The aggregate is composed of individual particles called primary particles of about 30 nm in diameter (reproduced from [54]).

Ultimately it is the surface of the soot that communicates to the surrounding environment, either for future growth, oxidation, or as a substrate for heterogeneous nucleation. These surface processes and the reaction kinetics determine soot size,, composition, mass and the surface area. This implies that we need both the tools, and methodology to characterize surface processes on soot. In what follows, we describe size resolved soot surface oxidation kinetics in a systematic manner. The soot surface oxidation kinetics in the presence of metals is also discussed. Studies are shown for three types of soot: diesel soot, bio-diesel soot and flame soot (carbon black).

1.1. Soot formation and growth

Soot formation is a multi-stage process which includes nucleation, coagulation, surface growth, aggregation, agglomeration and oxidation. At the initial nucleation stage the first condensed phase materials form from the gas species originating from the pyrolysis or oxidation products of the fuel molecules such as acetylene and PAH. This process leads to very small particles with diameters up to 2 nm which have only a small fraction of the total particulate mass ultimately formed.

Once soot nucleation has occurred, the amount of soot generated is determined by the competing processes of growth through the addition of gas-phase species, and destruction through oxidation by O_2, OH, and other gas-phase oxidants. In order to understand and model soot production, it is necessary to obtain a molecular level understanding of these processes. This includes, as a start, measuring oxidation and growth rates as functions of temperature and chemical composition. It is the purpose of the current study to present a new method for obtaining information on fundamental surface processes on nanoparticles, starting with the oxidation of soot in air.

1.1.1. Flame soot

The description of flame soot used in this study is as follows. The flame soot was generated in a Santoro type diffusion burner [5]. It consists of two concentric tubes: a 4 inch outer brass cylinder for air flow, and a 0.5 inch inner brass tube for fuel flow. Between the concentric tubes there is a honeycomb and a stack of beads and mesh to provide a uniform exit flow profile for the air. A 10 inch high glass cylindrical shroud is placed on the outer tube to prevent the flame from being disturbed by outside air currents. For the experiments presented in this paper, ethylene was used at a flow rate of 85 cc min^{-1} to produce a flame 50 mm high.

1.1.3. Diesel and bio-diesel soot

Biodiesel is a generic term that refers to various fatty-acid mono-esters that can be used as diesel fuel. It is made from the conversion of triglyceride (vegetable oil and animal fats) to esters (primarily methyl esters) via various esterification processes [6]. Biodiesel has very similar physical properties to conventional diesel fuel [7]; but is renewable, non-toxic, and biodegradable [8]. Biodiesel is the only alternative fuel to have fully completed the health effects testing requirements of the Clean Air Act. It may be made from a variety of different vegetable oils or animal fats. For example, in Germany rapeseed oil based biodiesel, RME, is the most abundant [9], whereas soy based biodiesel, SME, the fuel used in this study is the most widely used in the United States [10].

In general it is reported that biodiesel has a less adverse effect on human health than petroleum based diesel fuel. Schröder et al. [9] and Krahl et al. [11] reported that mutagenicity of biodiesel particulate emissions is much lower than that of petroleum based fuel. Finch et al. [12], in their study of rats exposed to biodiesel emissions, showed only modest health effects at the highest exposure level. Even these effects were described as "no-observed-adverse-effect" within the uncertainties of their study.

Europe is the most significant biodiesel producer in the world [13, 14]. Germany and France lead the production having tax benefit for producing biodiesel. In South America, Brazil launched national program for biodiesel in 2002 [15], leads the production and considers export of biodiesel to other countries [16].

1.2. Size measurement and resolution

Soot aerosol consists of a wide size distribution of nanoparticles and nanoparticle aggregates. The soot surface reaction kinetics is a strong function of the size and the surface area. Thus to study the size dependent reaction kinetics, a method is needed to separate soot nanoparticles with respect to the size.

Aerosol size distributions are commonly measured using differential mobility analyzer (DMA) that measures the electrical mobility of the particles. The electrical mobility is translated into mobility diameter for spherical particles by equating the drag on spheres to the electric force inside the DMA. For non-spherical particles such as soot nanoparticle aggregates (with low fractal dimension < 2), it is generally accepted that

the surface area calculated using the mobility diameter is close to the actual surface area of the particles[17].

1.2.1. Differential mobility analyzer

A differential mobility analyzer (DMA), illustrated schematically in Figure 2, is a class of ion-mobility spectrometer, which sizes or selects particles base on electrical mobility. The DMA consists of a center rod upon which a voltage is placed and an outer cylinder held at ground. The sheath flow is introduced at one end and flows coaxially between the outer cylinder and the inner rod. Aerosol particles enter the DMA in a thin ring adjacent to the outer cylinder, and the charged particles are attracted or repelled by the potential on the center rod. Near the end of the center rod is a slit through which particles of the desired electric mobility pass, while particles of higher electric mobility (particles that are smaller and/or more highly charged) hit the center rod upstream of the sample slit and particles of lower electric mobility (larger and/or

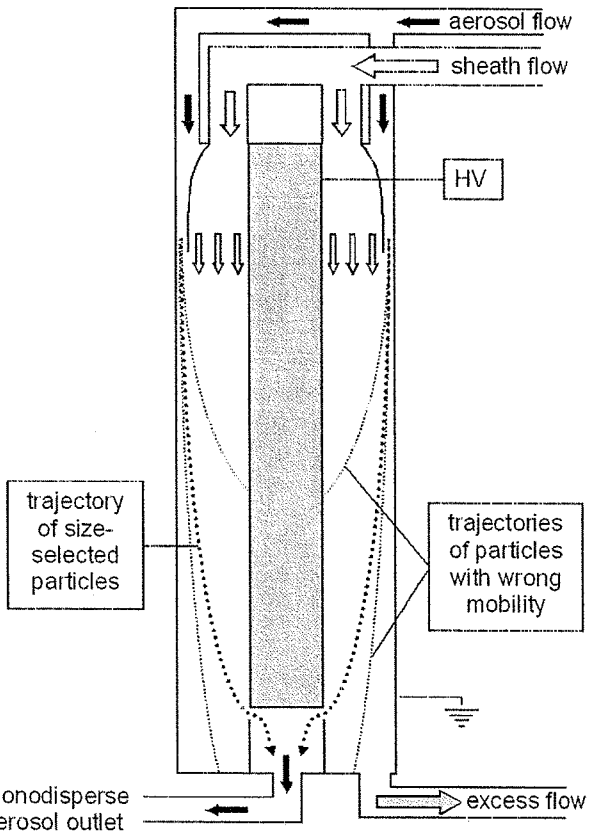

Figure 2. Schematic of differential mobility analyzer.

uncharged) pass out of the DMA through the excess output flow. If the DMA is used to select a particular particle size, the center rod is held fixed at a voltage and the sample output flow will contain only particles of a single electric mobility. In this mode the DMA acts like a high resolution band-pass filter. For the particle sizes used in the current experiments the vast majority of charged particles in a steady state charge distribution will carry a single charge, so the output aerosol will be essentially monodisperse. If the DMA is used to measure the size distribution of a particle stream, the voltage on the center rod is stepped and the sample output flow is monitored for particle concentration as a function of applied voltage.

As shown in Figure 1, soot particles are geometrically complicated agglomerates of smaller particles, therefore the meaning of size used here is not straightforward. In the free-molecular and transition regimes, where the particle size is smaller than or comparable to the mean free path of the gas molecules (~65 nm for air at room temperature and one atmosphere pressure), it has been shown that the particle mobility is inversely proportional to the mass transfer rate to the particle, which in turn is proportional to the gas-accessible surface area of the particle [18-20]. Therefore, for the particle sizes under consideration in this work, the DMA will select particles based on their accessible surface area. The particle size is still described by a mobility diameter, D_p, which is the diameter of a spherical particle of equivalent mobility, and therefore of the same surface area.

1.2.2. Tandem differential mobility analyzer

The term "tandem" is used for a DMA (usually identical) which is placed downstream of another DMA. The tandem DMA (TDMA) system can be used for online monitoring of size changes occurring by some process condition imposed between the two DMA's. In this manner the TDMA system operates much like a MS-MS system. For example, a DMA classified aerosol stream can be passed through a tubular furnace at an elevated known temperature whereby the aerosol undergoes a change in mobility due to processes like oxidation, sintering, or change in charge state [21]. The resulting mobility change can be measured by a second DMA, which can be related to a change in size or charge. If the process time and chemistry is known then the size change can be used to measure the process kinetics.

Figure 3 shows the TDMA system [22] for measuring oxidation kinetics of freshly generated and size-selected soot nanoparticles. The TDMA method as described in section 2.2, was advantageous because for freshly generated soot, effects of aging and transport/diffusion of the reactant can be minimized.

1.3. Soot oxidation and kinetics

We define the mass based oxidation rate as:

$$\frac{dm_s}{dt} = -\dot{w}A_s \tag{1}$$

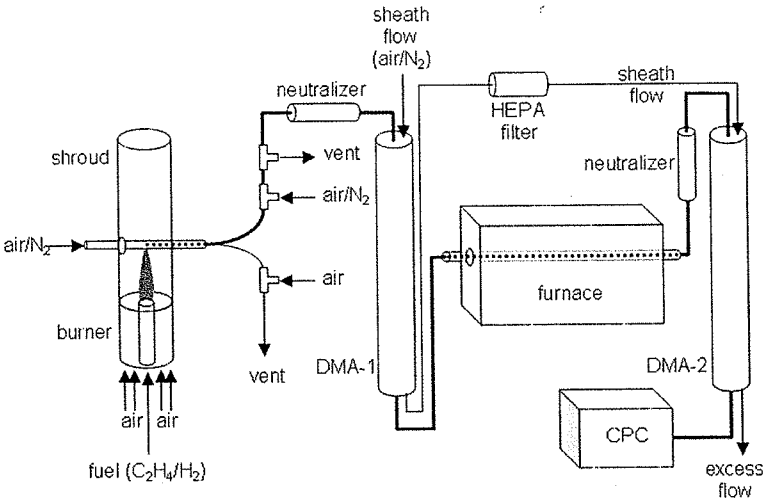

Figure 3. Soot oxidation kinetics measurements using TDMA system. The bold line indicates the path taken by the soot aerosol particles.

with A_s the soot surface area and $\dot{w}$ is the mass-based surface specific rate, often modeled using a modified Arrhenius expression,

$$\dot{w} = AT^{1/2} \exp\left(\frac{-E_a}{RT}\right) \tag{2}$$

where A is size independent preexponential factor, E_a is an activation energy, R is gas constant, and T is temperature in Kelvin.

For a non-uniform axial-temperature profile in a flow reactor the diameter change can be integrated as a particle travels the length of the reactor:

$$\Delta D_p = 2\int_0^X \frac{\dot{w}(x)\tau(x)}{\rho_s} dx \tag{3}$$

where x is the axial distance in the reator tube and X is the length of the reactor tube. The dependence of the rate and residence time on horizontal position is a result of their dependence on temperature,

$$\frac{\dot{w}}{\rho_s} = A_{nm} \cdot [T(x)]^{1/2} \cdot \exp\left[-\frac{E_a}{RT(x)}\right] \tag{4}$$

$$\tau = \tau_o \frac{T_o}{T(x)} \tag{5}$$

where A_{nm} is a different frequency factor for each initial soot particle size, E_a is the activation energy, and τ_o is a characteristic residence time at temperature T_o. The residence time is calculated assuming laminar flow and a flow velocity equal to the peak volumetric flow velocity of 4/3 u_m, where u_m is the mean flow velocity calculated from

the volume flow rate and the cross-sectional area of the flow tube. The flow velocity as a function of axial position can be written as

$$u(x) = \frac{4}{3} u_m \frac{T(x)}{T_o} \tag{6}$$

2. SOOT OXIDATION KINETICS MEASUREMENTS

Soot oxidation kinetics is measured by both offline and online methods: (a) the offline method employs direct visualization using TEM analysis, (b) the online method uses TDMA system.

2.1. Offline method: TEM observations

The soot oxidation was qualitatively visualized by Tanaka [23] using TEM analysis of diesel soot collected on a thin Al_2O_3 plate. Tanaka [23] observed the size change of an agglomerate and found that each of the primary particles gets smaller as it is oxidized. In this section we extend Tanaka's [23] method and describe a method to quantify soot oxidation: An experimental protocol is described to measure the oxidation rate of soot particles at low temperatures (< 800 K) using TEM image analysis.

2.1.1. Method

The size-selected soot particles were deposited on TEM grids. A section of TEM grid containing a number of particles sufficient to provide statistically meaningful data was selected. A series of TEM images taken using a digital CCD camera from low to high magnification are shown in Figure 4. A map of the grid was made. The grid is then removed from the TEM and inserted into a furnace for a specified time and temperature. The soot particles on the TEM grid were oxidized in heated air for the given time and temperature. Analysis of the oxidation exposed grid used the same field of view as was used prior to oxidation using the procedure illustrated in Figure 4. The projected area change is related to the surface specific reaction rate for soot oxidation. The projected area determined using a public domain image program (NIH *Image*).

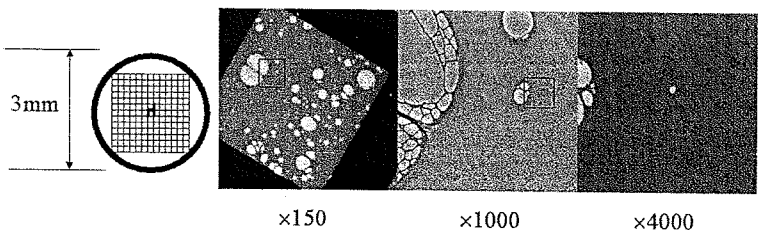

Figure 4. Maps of TEM images to track a field of view.

2.1.2. *Visualization of soot oxidation- Tracking individual particles*

Figure 5 shows examples of individual particles during oxidation at different cumulative oxidation time at 450 °C. Initial images of particles (a) and (e) were taken and those particles were tracked separately. The soot aggregates are composed of primary particles in 20-30nm size range. Clearly the primary particles are shown shrinking during this process, but we also observe that some changes in the aggregate morphology. The latter observation presumably has to do with how the particles find themselves anchored to the grid, and one might expect differences from what might occur in the gas phase. Most of the primary particles were observed to shrink evenly during oxidation. For these particular images an arm of the aggregate seemed to move during oxidation (Figures 5a-d) whereas the particle in Figures 5e-h shrank in size without significant changes in shape.

The individual particles can undergo different projected area reduction rates due to the following reasons:

A. A portion of a particle can disappear during oxidation.
B. The oxidation rate can be different due to differences in chemical composition for individual particles).

Thus, in the following sections, we track a group of particles rather than individual particles to quantify the oxidation rate.

2.1.3. *Comment on hollow particles*

Our more gradual evolving particle shape and size is in contrast to Heckman's [24] observation. He employed high temperature heat treatment (partial graphitization in an inert atmosphere) before carrying out an oxidation experiment. His work found very

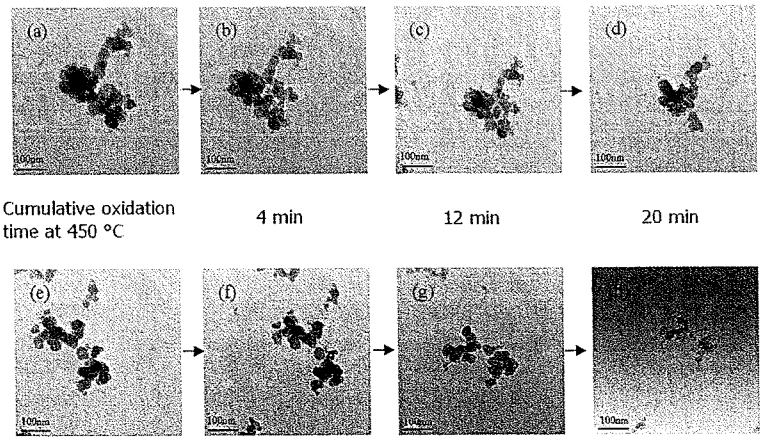

Figure 5. TEM images of individual particles during oxidation at different cumulative oxidation time at 450 °C.

little shrinking, but rather an internal hollowing out of the particles. He speculated that a more ordered graphitic layer structure, at the surface of the particles was stable against oxidation, and Gilot et al. [25] also reported internal oxidation of carbon black spherules after 60% burn-off at low temperature. We observed no selective hollowing of soot particles in this study, which we believe is related to the absence of a pre-graphitization process [26].

2.1.4. *Visualization of soot oxidation- Tracking a group of particles*

A field of view containing about 100 particles was chosen for tracking during oxidation. In order to observe such a large number of particles in a single image the magnification used (×4000~×5000) is about 6 times lower than that used for tracking individual particles and is shown in Figure 6a. Figure 6b shows the image after oxidation in a furnace for 4 minutes at a furnace set temperature of 450°C. Qualitatively we see that particles are clearly shrinking, but some particles are oxidizing faster, and in some

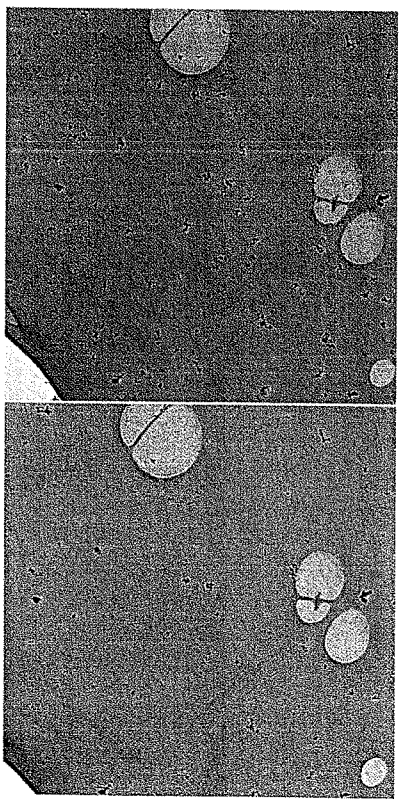

Figure 6. TEM images before and after oxidation for a group of particles. (a) Size classified soot particles before oxidation (d_m=50nm). (b) After oxidation (4min at 450 °C of furnace set temperature).

cases particles disappeared entirely. These differences in oxidation rate would seem to indicate that even though all particles were sampled from a single location and size segregated with a DMA, they may not be chemically the same. Particles that disappeared were excluded manually during image analysis so that the exactly same group of particles could be tracked.

Figure 7 shows the resulting size distributions for particles in Figure 6 using the data analysis procedure described. Both the size distributions were broadened and shifted towards lower sizes. In the following section, the change in size is quantified by relating the projecting area equivalent diameter to the mobility equivalent diameter.

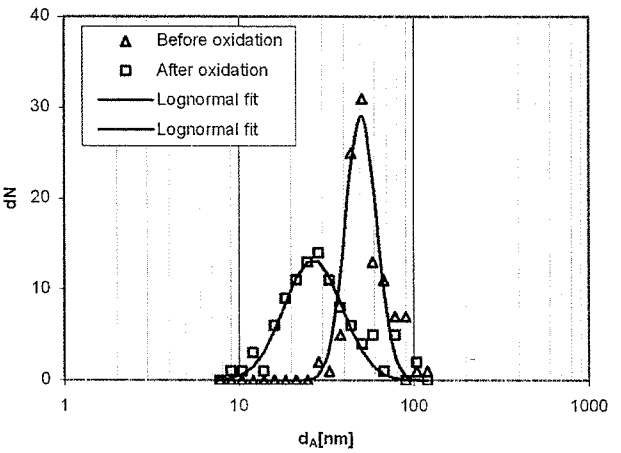

Figure 7. Size distributions based on projected area equivalent diameter for particles shown in Figure 6.

2.1.5. Projected area equivalent diameter vs. mobility equivalent diameter

The mobility equivalent diameter (d_m) is based on the DMA measurements and the projected area equivalent diameter (d_A) is based on the TEM measurements. In order to quantify these size changes, it is necessary to establish a relationship between the two diameters. The DMA was used to classify particles with mobility diameters: 50nm, 100nm, 130nm, and 150nm. The TEM samples for each selected size were taken. It is assumed that both d_A and d_m, are orientation-averaged properties, since the agglomerates are expected to rotate randomly in a DMA column, and in an impactor. Figure 8a, shows size distributions of the TEM samples for a given mobility diameter as a function of d_A. Figure 8a shows that the selected mobility size from the DMA (50nm) coincides with the peak of the projected area equivalent diameter obtained by analyzing the particles on the TEM grid. The second peak (at 75nm) corresponds to particles of the same electrical mobility but with two charges. Figure 8b shows a mobility size distribution measured using the TDMA method with the furnace turned off. The peak, which is around 75nm in d_m as shown in Figure 8b, represents particles, which

were doubly charged when they passed through the DMA-1 but singly charged when they passed through the DMA-2.

The excellent agreement between Figure 8a,b confirm that d_m is effectively equivalent to d_λ in the size ranges of interest to this study. The TEM data is noisier because we limited the analysis to only 100 particles, while the DMA effectively is sampling several orders of magnitude of particles. Similar results were obtained for mobility diameter 100, 130 and 150 nm. For these measurements, the relationship between d_m and d_λ is shown in Figure 9. It is found that the mobility diameter scales linearly with the projected area equivalent diameter with a slope of unity.

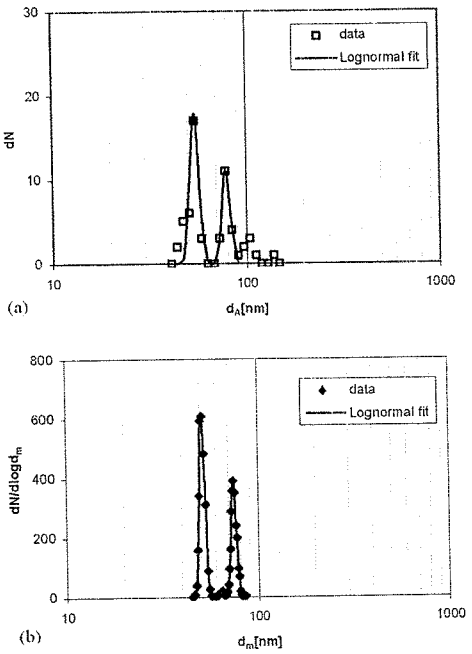

Figure 8. Comparison between size distributions measured as a function of projected area equivalent diameter (d_λ) and as a function of mobility equivalent diameter (d_m) for a given mobility diameter selection (d_m=50nm) by a DMA. (a) TEM measurement. (b) TDMA measurement.

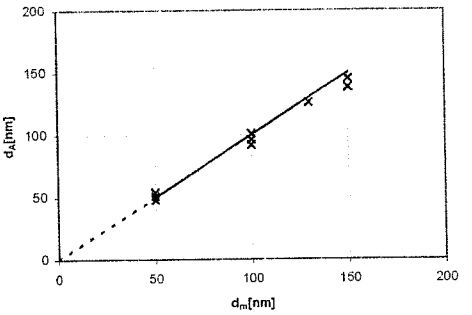

Figure 9. The relationship between projected area equivalent diameter (d_λ) and mobility equivalent diameter (d_m) for soot agglomerates. $d_m/2\lambda$ is the normalized particle diameter by 2λ, where λ is the mean free path of the carrier gas.

2.1.6. Determination of the soot oxidation rate

As we see in the previous section, d_m and d_A are equal for the set of experiments discussed in this study. Thus d_A can be replaced by d_m for calculating the rate of oxidation.

The surface area for mass transfer of the soot particles in the free molecular regime is πd_m^2. By definition the effective density is

$$m_s = \rho_{effective} \frac{\pi d_m^3}{6} \tag{7}$$

After mass and area are expressed in terms of the mobility equivalent diameter, Eq. (1) becomes

$$\frac{dd_m}{dt} = -\frac{2\dot{w}}{\rho_{effective}} \tag{8}$$

The effective density is assumed constant and equal to 1800 kg/m^3 (Kennedy [27]). Eq. (8) can be integrated over time as follows:

$$\Delta d_m = \Delta d_A = \int_0^t -\frac{2\dot{w}(t)}{\rho} dt \tag{9}$$

Using experimental data on the change in d_A at different furnace set of temperatures, a least-square fit was carried out to determine A and E_a for $\dot{w}$.

For the low temperatures (< 800K) discussed in this study, the soot oxidation activation energy was found to be ~148 kJ/mol. The surface area specific oxidation rate of soot particles at temperatures below 800 K is higher than found in prior studies: A comparison is discussed in the next section. Further work is necessary to identify what caused the difference between low and high temperature oxidation rates.

2.2. Online method

2.2.1. Size selected TDMA measurements

Soot particles were generated in an ethylene diffusion flame. Samples for TEM analysis were collected directly in the flame or in the sampling stream. The TEM images shows that the soot particles were agglomerates of spherical particles, with primary particle diameter of about 20-30 nm.

The size distributions were measured using a DMA. The DMA was also used as an electrostatic classifier to separate particles in a given mobility diameter range. The mono-disperse soot particles were oxidized in the presence of air at a high temperature inside a tube furnace. The resulting changes in mobility diameter were measured using a second DMA. The experimental system is shown in Figure 3.

In order to check for size reduction due to thermal effects such as particle collapse, rearrangement, or evaporation, experiments were run with the furnace set at 1100° C using nitrogen as the soot sampling carrier gas, the dilution gas, and as the sheath gas for the two DMAs. All other conditions were kept the same as for the oxidation experiments.

The TDMA scans for the oxidation in air of the three initial soot particle sizes are presented in Figure 10. The initial ~1% decrease in D_p at 500° C for all three particle sizes was most likely due to volatile or semi-volatile material evaporating off of the particles, and the size decrease due to oxidation is calculated relative to the particle sizes at 500° C. An increase in the width, or spreading, of the size distributions as oxi-

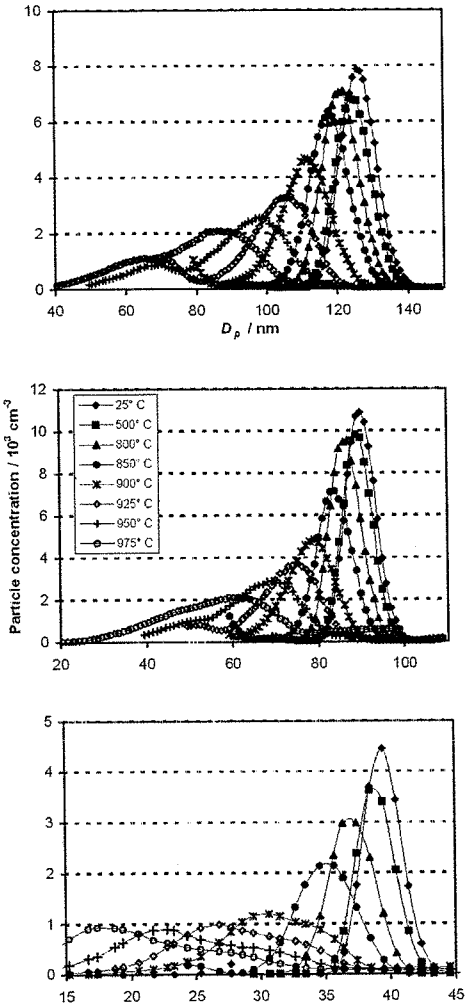

Figure 10. TDMA soot oxidation results in air for furnace settings of 25° to 975° C (see legend). Results from higher furnace settings are omitted for clarity. (a) 40 nm initial particle size, (b) 90 nm initial particle size, and (c) 126 nm initial particle size.

dation occurs can be seen in Figure 10, along with the appearance of a bimodal distribution at higher temperatures for the 40 nm particles. What appears to be a bimodal distribution for the larger particles is actually a blending of the peak due to singly-charged particles with the peak due to doubly-charged particles.

The decrease in particle size assuming spherical particles and no density change during oxidation is

$$\Delta m_s = \frac{\pi \rho_s}{6}\left(D_{p,i}^3 - D_{p,f}^3\right) \tag{9}$$

where m_s is the soot particle mass, ρ_s is the mass density of a soot particle, and D_p is the mobility diameter of a soot particle. Assuming spherical soot particles and integrating Eq. 1 over the residence time τ, we get

$$\dot{w} = \frac{\rho_s \left(D_{p,i} - D_{p,f}\right)}{2\tau} \tag{10}$$

Eq. 10 suggests that the surface specific rate is linearly proportional to the change in diameter. Thus given experiments at a series of constant temperatures and a known residence time in the reaction region, one can calculate the activation energy and pre-exponential factor using the standard Arrhenius equation (Eq. 2).

A non-linear least-squares fit to the experimental data was performed by numerically integrating Eq. 10 for each furnace setting and initial particle size combination. Temperature profiles for furnace settings other than 800° or 1000° C were estimated using a linear interpolation or extrapolation of the points measured using the shielded thermocouple at 800° and 1000° C, while interpolation for a specific furnace setting was performed by fitting the points measured at specific distances in the flow tube to a sixth-order polynomial. Figure 11 presents the observed and calculated size decreases of the soot particles.

The activation energy was found to be 162 kJ/mol. An attempt was made to fit the exponent of the temperature in Eq. (4), but this was highly correlated with the A_{nm} parameters and therefore not determinable from our data. Also, fitting with a single size-dependent A parameter was attempted, but no adequate functional dependence on particle size could be found to fit the data for all three initial particle sizes. This indicates that the differences in oxidation rate observed for the three initial particle sizes is most likely more a function of the initial particle structure rather than the particle mobility size measured by the DMA.

The largest uncertainty in the present experiments comes from the assumption of laminar flow. This may not be too inaccurate, because the laminar flow assumption results in a spread in particle residence times. Experimentally, the observed spread in

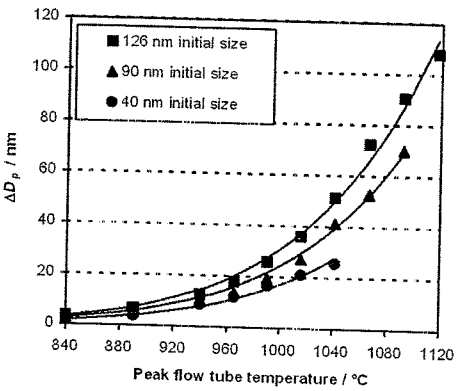

Figure 11. Particle size change as a function of peak flow tube temperature for the three initial particle sizes. Solid lines show size change calculated from the fitted model.

the size distributions is in line with the later residence time assumption. In such cases, if we assume that the uncertainty in residence time is linearly proportional to the residence time, then it translates linearly into an uncertainty in the A_{nm} parameters without affecting the activation energy.

There is a factor of 1.7 difference between the measured oxidation rates of the 40 and 126 nm particles. This may be due to a difference in the effective densities of the soot particles, or in the chemical composition of the particles. Because of the agglomerate structure of the soot particles, the effective density of the larger particles is lower than that of the smaller particles. This could lead to a higher rate of observed size reduction for the larger particles. Preliminary experiments in altering the soot composition indicate that increasing the amount of hydrogen in the soot leads to a higher oxidation rate. It can be conjectured that the different size particles have had different histories within the flame, and thus different elemental composition can be expected.

2.3. Comparison of oxidation rates based on TEM observations and TDMA measurements

In this section, we verify, both online and offline kinetics measurements against each other. The comparison between the two methods is made. A comparison of size distributions at 25 C (room temperature) and a furnace temperature of 1000°C is presented in Figure 12. The two experimental methods show excellent agreement in the most probable particle diameter before and after oxidation. Furthermore it provides another validation for the equivalence of d_A, and d_m.

Figure 13 shows Arrhenius plots of the surface specific oxidation rate for our measurements and prior studies. The activation energy of low temperature flame soot oxidation, was determined to be 148 kJ/mol by TEM method and is consistent with the 143 kJ/mol used in the Nagle and Strickland-Constable (NSC) [28] oxidation model (curve "d" in Figure 13) as extracted by Stanmore et al. [29]. However, our oxidation rate is an order of magnitude higher, than the extrapolated NSC model and even more than that for the other studies presented in this temperature range. To assess the possibility that this experimental approach somehow results in a higher observed reaction rate, we conducted an experiment under the same conditions (i.e. higher temperature) as our TDMA oxidation measurement. The results are shown in Figure 13 as the open circle, and overlaps with excellent agreement with our TDMA measurements [30], rate curve "c". The agreement suggests that the TEM sizing approach should be yielding accurate results at the lower temperature conditions.

To assess other possibilities for our higher rate, the soot sampled on the TEM grid was pretreated under a N_2 environment at 550 C for 5 min from which no noticeable size change was observed.

Another possibility considered was that the soot which was in contact with the SiO_2 TEM grid might somehow accelerate oxidation, however van Doorn et al. [31] have shown that SiO_2 has no catalytic effect on diesel soot particles. One may expect a lower activation energy along with an increased rate if catalytic effects are important as

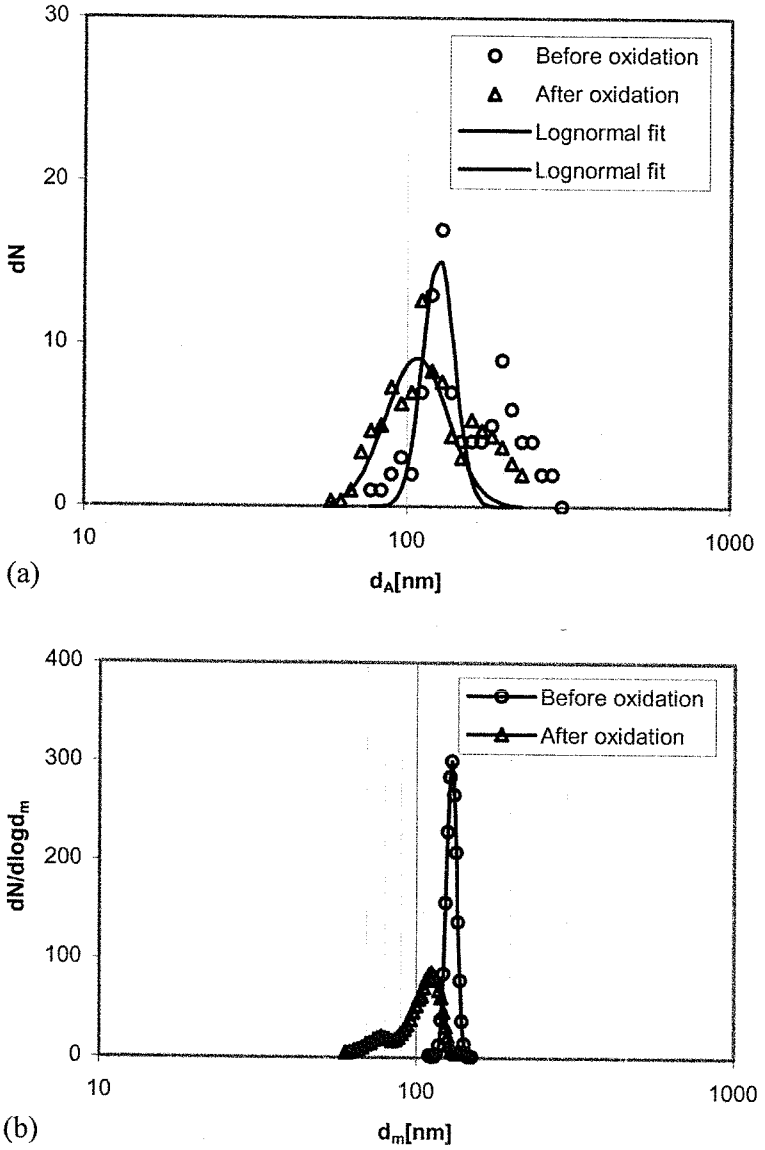

Figure 12. Comparison of (a) TEM and (b) TDMA measurements: The number distributions are shown before and after soot oxidation at 1000 °C.

observed by Miyamoto et al. [32]. In their work they saw enhanced rates for calcium laden diesel soot of up to 2 orders of magnitude higher (curve "e" in Figure 13) as compared with undoped soot (curve "f" in Figure 13).

Temperature is one of the most sensitive variables in determining reaction rate. Our uncertainty analysis indicates an uncertainty of $<\pm$ 2 K. If one were to assume a

worst case scenario and assume an uncertainty ten times larger, the resulting effect on the rate is shown in Figure 13, as the thin lines above and below rate curve "a". Obviously uncertainty in temperature cannot explain our observed higher rate.

The uncertainty related to the image analysis in the measurement of a 20 nm diameter is expected to be less than ±2nm. However, for particle below 20 nm, the uncertainty increases due to a decrease in the number of pixels which constitute a given particle. The dotted lines seen in Figure 13 "a" show ±1σ confidence lines. The propagation of the uncertainty in determination of d_λ to the final rate is negligible, since it lies within the confidence lines limits above.

Stanmore et al. [29] in their recent review has discussed the variation in the measured oxidation rates, some of which are presented in Figure 13. They suggested the possibility that some of the measured rates might be corrupted by mass transfer effects which would tend to make the observed rate lower. We should also note that

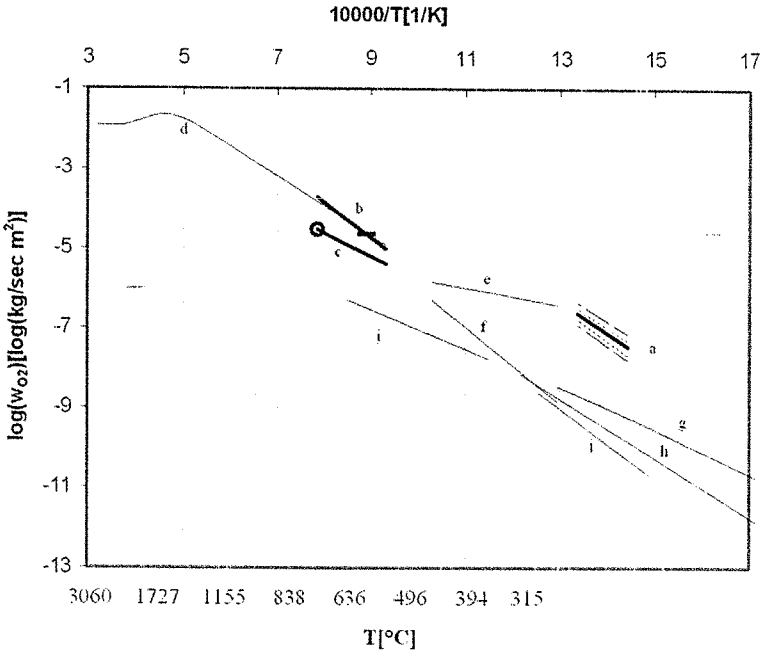

Figure 13. Arrhenius plot of the surface specific rates of soot oxidation for the current study and for other relevant prior studies. Previous studies produced a variety of activation energies, as can be seen by the varying slope of the lines. Results are presented for 21% O_2. (a) Flame soot by TEM method (—), rates for ±1σ confidence lines (—), rates for ±20K variation (—). (b) Flame soot by TDMA method (c) Diesel soot (d) Nagle and Strickland-Constable using a pyrographite rod (e) Miyamoto et al. TGA of catalyzed (Ca added to fuel) Diesel soot. (f) Miyamoto et al. TGA of uncatalyzed Diesel soot. (g) Ahlström and Odenbrand flow reactor study of Diesel soot. (h) Otto et al. TGA of Diesel soot. (i) Gilot et al. thermogravimetric analysis (TGA) of carbon black. (j) Neeft et al. flow reactor study of Printex-U flame soot from Degussa AG.

in the low temperature range, curve "j" reflects results for black carbon, while curves "h and g" are Diesel soot results from Otto et al. [33], and Ahlström and Odenbrand [34], respectively. This difference in source may also create differences in measured rates.

Ishiguro et al. [35] studied the microstructure evolution for Diesel soot oxidation at about 800 K using an analytical electron microscope. During oxidation they observed flaking of crystallites from the outer most shell of the particles. This would certainly make the apparent rate higher than NSC prediction, however that does not explain the discrepancy between our results and the other low temperature data. Furthermore, given the resolution of our instruments we were not able to assess if this flaking phenomena was taking place for our particles.

We conclude that the measured higher rate by TEM method is attributed to a measurement protocol that more effectively assesses the intrinsic chemical reactivity, without the corruption of heat and mass transfer effects associated with bulk methods. These results are consistent with our single particle mass-spectrometry studies on condensed phase chemical kinetics, much higher reaction rates were observed for small particles over bulk samples [36].

2.4. Bio-diesel soot kinetics

In this study the kinetics of particle oxidation are measured for particles emitted by a diesel engine operating on a 100% soy methyl ester (SME) biodiesel fuel (B100). The TDMA method described in section 2.2 is employed to measure surface-specific oxidation rates from size-selected diesel exhaust particles over the temperature range of 700 to 825 °C. The change in particle diameter after oxidation took place was measured and converted into the surface specific oxidation rate using method described in section 1.3.

Figure 14 shows representative TDMA data for 89 nm particles generated using biodiesel at 1400 RPM, 75% load. Results for the other initial particle sizes tested (40 and 128 nm) are not presented here but are similar. Figure 14 illustrates that the particles shrink as the furnace temperature increases, and that the mobility diameter decreases by 2 nm at 500 °C and 9 nm at 800 °C.

The initial shrinkage in size below 500 °C is likely due to desorption or evaporation of volatile materials. We previously [37] found that the total particle size decrease, due to non-oxidative effects at 500 °C, measured using nitrogen as the carrier gas, amounted to ~1 nm at 75% load using regular diesel fuel. The larger 2 nm shrinkage we observed at 500 °C using biodiesel can be attributed to the presence of more volatile PM with biodiesel. Above 500 °C, most of the change in diameter is a result of particle oxidation. In addition to a decrease in particle size with increasing oven temperature, we also observed a decrease in the number of particles. This decrease is not associated with chemical reactivity, but rather, it is associated with thermophoretic transport losses, which become more important at higher temperatures [38].

Figure 15a shows experimentally determined size reductions at various oxidation temperatures for 40, 89 and 128 nm. For comparison purposes, Figure 15b shows results from our prior oxidation work using regular diesel fuel [37]. In both cases, we

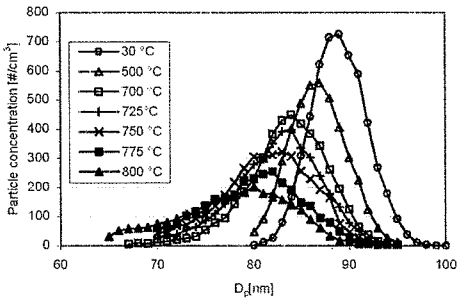

Figure 14. TDMA diesel particle oxidation results in air for furnace settings of 30-800 °C. 89 nm initial particle size with B100 biodiesel at 1400 RPM, 75% load.

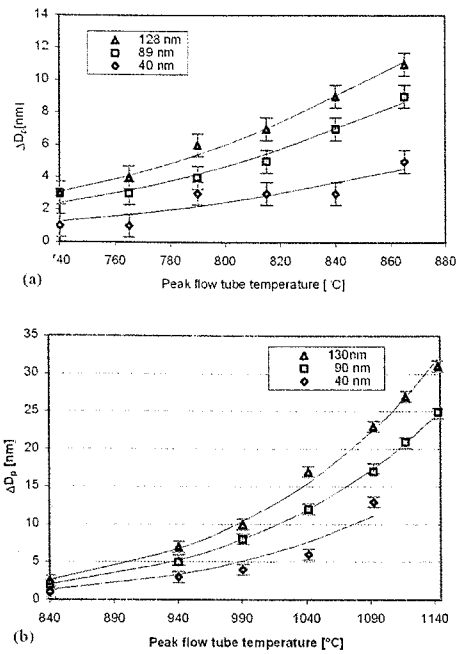

Figure 15. Particle size change as a function of peak flow tube temperature for the three initial particle sizes. (a) B100 biodiesel. (b) D2 fuel [37].

observed an increase in the apparent oxidation rate with increasing initial particle size. That result was investigated in our previous study [37]. It is necessary to correct the rates for the effective density of soot, which was measured [39] using an Aerosol Particle Mass analyzer. We [39] observed that the effective density increases as the particle size decreases. Normalization to the effective density using their data resulted in an oxidation rate that was essentially particle size independent [37].

For practical convenience, we define the light-off temperature of oxidation as the peak-flow tube temperature, where the particle shrinks ~1 nm (beyond that due to thermal evaporation). This is not the same as the light-off or balance point temperatures used in describing DPF performance which are generally much lower than those observed here. The difference is due to the much shorter reaction times, about 1s, used in our experiments compared to DPF regeneration times. Our light-off temperatures are a fundamental measurement of particle reactivity in a system not constrained by heat and mass transfer effects. The light-off temperature was determined to be ~ 840 °C for the regular diesel (D2) particles as shown in Figure 15b, but decreased significantly to 740 °C for biodiesel, as shown in Figure 15a. The data in Figure 15a were fitted to an Arrhenius expression (Eq. 1). The activation energy was 88.5 kJmol^{-1}. The A_{nm} factors were 0.77, 1.5 and 1.9 ($\times 10^4$) nm K$^{-1/2}$s^{-1} for 40, 89 and 128 nm mobility diameter aggregates.

2.5. Role of metals

In this section, the role of metals in soot oxidation is examined. Diesel soot and flame soot are discussed. As shown in previous sections, the oxidation kinetics of these two types of soot differs. It is hypothesized that the presence of metals in diesel possibly coming from the lubricating oil leads to a higher oxidation rate. Furthermore, recent studies show that metal based fuel additives can lower the particulate emissions and enhance oxidation rates. In these works, a variety of metal additives have been tested. Miyamoto et al. [32, 40] investigated the effect of Ca, Ba, Fe, and Ni naphthenates. They found Ca and Ba most efficiently reduced the soot, by both suppressing soot formation and enhancing soot oxidation. Valentine et al. [41] studied the catalytic effect of bimetallic Pt/Ce additives in an attempt to lower the dosing level of the metal additive down to 4 ppm to reduce ash loading on the diesel particulate filter (DPF) and the emission of metallic ultrafine particles. Skillas et al. [42] studied the effect of Ce and Fe on the size distribution and composition of Diesel PM; they observed a reduction in the accumulation mode, but an increase in ultrafines. Lahaye et al. [43] studied the catalytic effect of Ce on simulated Diesel PM oxidation and observed that the cerium was both on and within the soot as cerium oxides. Kasper et al. [44] added ferrocene to the fuel and speculated that the enhancement of oxidation was more effective in reducing soot than a suppression effect.

Many studies [45, 46] have focused on the change in ignition temperature of the Diesel PM bed with different metal additives. While these results are of obvious practical benefit, it has been difficult to decouple the role of the catalyst on the increase in the oxidation rate from other effects that may also promote an increase in oxidation rate and a decrease in ignition temperature (i.e., the heat and mass transfer effect, particle size, etc.).

In view of the complex interrelationships discussed above, we have attempted to extract intrinsic oxidation kinetics in the following sections, in order to assess the role of the catalyst in the enhancement of the oxidation rate. First, the role of cerium additive on the diesel soot oxidation is discussed. Then, the role of metals in diesel soot oxidation is examined against iron-doped flame soot oxidation.

2.5.1. Influence of cerium additive on the size distribution

Figure 16 shows the effect of the cerium additive on the particle size distribution for various dosing levels at fixed engine condition (75 % engine load (300 N m) at 1400 RPM). The addition of the cerium additive clearly had a significant effect on reducing the number concentration of particles in the accumulation mode. A 50 % reduction in peak concentration was observed at the 25 ppm dosing level, which was further reduced to 65 % with 100 ppm of additive. The relative insensitivity of the results to dosing level was qualitatively consistent with work from Skillas et al. [42]; they found significant reduction of particles in accumulation mode at 20 ppm of cerium, but did not see any noticeable effect of further increases in cerium additives. While the accumulation mode clearly decreased, a dramatic increase in the nuclei mode was observed with the addition of cerium, which has also been confirmed by Skillas et al. [42]. This behavior

is consistent with particle physics. A decrease in the accumulation mode, and therefore available surface area, as shown in Figure 16b, reduces scavenging of particle precursors, thus promoting homogeneous nucleation, while at the same time decreasing coagulation of nuclei mode particles with accumulation mode particles.

2.5.1.1. TDMA results

The experimental system is described by Jung et al. [47]. Figure 17 shows representative TDMA data for 90 nm particles generated under 25 ppm cerium added fuel, at a fixed engine condition (75 % engine load (300 N m), 1400 RPM). Results for other initial particle sizes at 25 ppm and 100 ppm cerium doping were similar to those presented in Figure 17. The particles shrink as the furnace temperature increases and the mobility diameter decreased by 1 nm at 300 °C and 7 nm at 650 °C. The total particle size decrease, due to non-oxidative effects at 500 °C, measured using nitrogen as the carrier gas, amounted to ~1 nm at 75 % load using regular diesel [37]; this is consistent with the shrinkage we observed at 300 °C for cerium loading. The initial shrinkage in size below 300 °C is inconsistent with the kinetic results observed at higher temperatures and is likely due to the evaporation of semi-volatile materials condensed on the diesel particles. Sakurai et al. [48] have also reported such shrinkage. Above 300 °C,

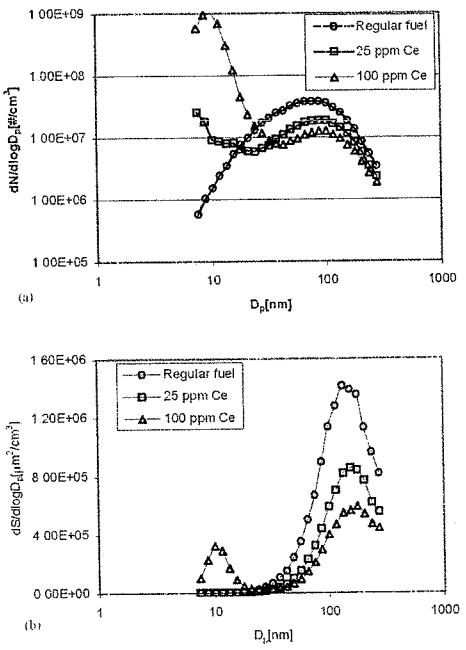

Figure 16. Size distributions of diesel particles with cerium dosed fuel for various dosing levels at 1400 RPM, 75 % load. (a) Number distributions. (b) Geometric surface area distributions.

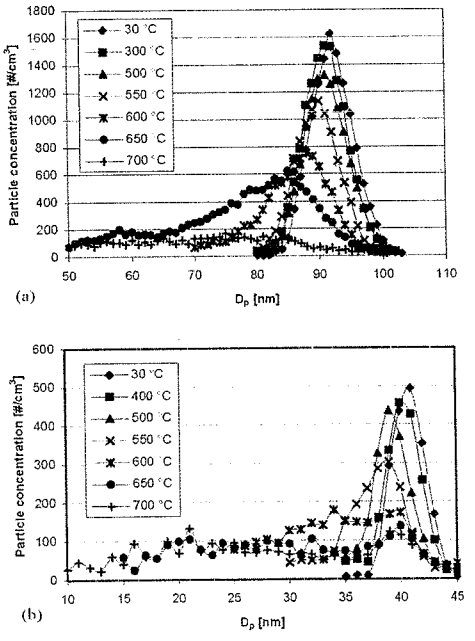

Figure 17. TDMA Diesel particle oxidation results in air for furnace settings of 30-700 °C. (a) 92nm initial particle size with 25 ppm cerium dosed fuel. (b) 41nm initial particle size with 100 ppm cerium dosed fuel.

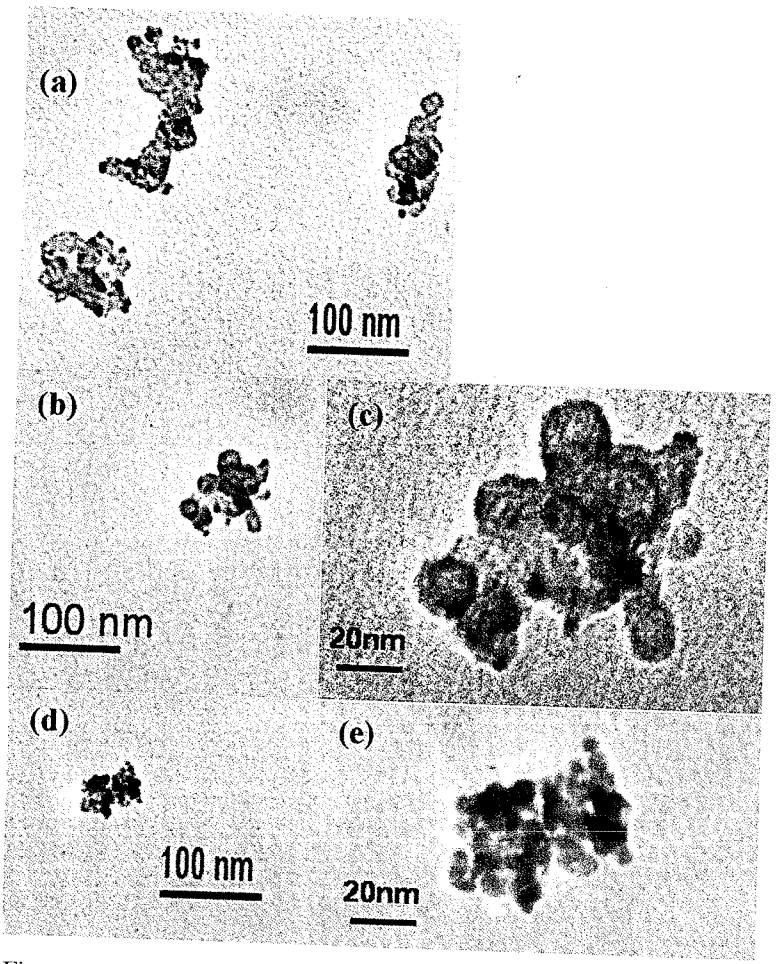

Figure 18. TEM images of 50 nm mobility diameter selected cerium-laden diesel particles. Samples are taken under the condition of 75 % load at 1400 RPM using 100 ppm cerium doping level. (c) and (e) are at higher magnification.

most of the diameter change results from particle oxidation. In addition to a decrease in particle size with increasing oven temperature, we also observed a decrease or loss of particles. This decrease in number concentration was not associated with chemical reactivity, but rather, thermophoretic transport losses, which become most important at higher temperatures [49]. In Figure 19b, we see results for 40 nm particles at 100 ppm cerium doping. At higher oven temperatures, two modes were observed. In this case, rather than a steady decrease to smaller sizes by the primary peak, as observed in all our previous studies, here we saw a mode (e.g., at 600 and 650 °C) near 40 nm, and another peak at about 34 and 32 nm, respectively. This behavior may be attributed to some particles being primarily composed of cerium compounds that homogeneously condensed from the vapor and have an associated carbon coating. The mixture of 40

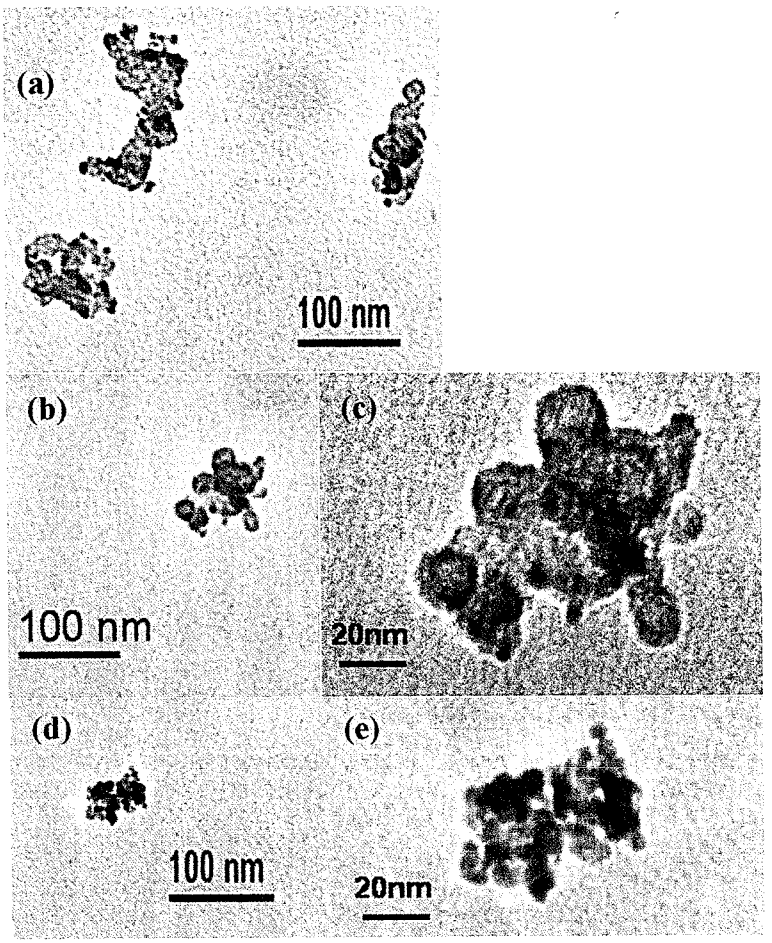

Figure 19. TEM images of 130 nm mobility diameter selected of cerium-laden diesel particles. Samples were taken under the condition of 75% load at 1400 RPM using 100 ppm cerium doping level. (b) and (c) at higher magnification compared to (a).

nm, predominately either cerium or carbon, resulted in a bimodal size distribution after oxidation. This is consistent with the TEM observations discussed below.

Figures 18 and 19 show TEM images of cerium-laden-diesel particles under 75%, 1400 RPM at 100 ppm cerium doping level. Sampling particles on SiO_2 coated nickel TEM grids follows the procedure detailed in our previous study [50]. In brief, the aerosol flow after the 1st stage of the dilution tunnel was sent to a DMA and the resulting monodisperse output was sent to a Low Pressure Impactor (LPI)[51]. Particles were collected on the TEM grid at the bottom stage of the LPI.

Referring to Figure 17b, we observed a bimodal distribution after oxidation at 700 °C. The first mode consists of pre-selected 40 nm particles that remained after oxidation, while the other mode reflects shrinkage to ~ 20 nm. This is consistent with

some particles exiting the engine being primarily composed of metal, as seen in Figure 18d.

Size decreases due to oxidation were determined relative to the size of the particles at 300 °C. This is lower than the temperature of 500 °C which we used in our previous studies [37, 49]. Lowering the base temperature was necessary because of the increased reactivity of the diesel particles by the addition of metal additives.

2.5.1.2. Kinetic rates

Figure 20 shows experimentally determined size reductions at various oxidation temperatures for 41, 92 and 132 nm particles at 25 ppm (Figure 20a) and 100ppm (Figure 20b) cerium doping levels. Figures 20a,b can be compared with Figure 15b for undosed Diesel oxidation in Section 2.4. One of the obvious differences seen between this work and the undosed results is that we did not see any size dependant oxidation. In the undosed case, we observed an increase in the apparent oxidation rate with increasing initial particle size. That result was investigated in our previous study [37] to correct the rates for the effective density of soot, which was measured by [39] using an Aerosol Particle Mass analyzer. Park et al. [39] observed that the effective density increases as the particle size decreases and that normalization to the effective density resulted in an effective oxidation rate that was essentially particle size independent [37]. At this point, we do not have a definitive explanation of the differences observed between the dosed and undosed cases; however, it is possible that the nature of the soot structure in the dosed case is different and it is also possible that the mass fraction of cerium in the soot particles is size dependent. All that can be concluded without further investigation is that the apparent oxidation rate for dosed Diesel is size invariant.

The light-off temperature was determined to be ~ 840 °C for the undosed Diesel particles as shown in Figure 15b, but decreased significantly to 540 and 590 °C respectively, for the 25 ppm and 100 ppm dosing level, as shown in Figures. 20a,b. The results suggest that the catalyst fulfilled a major, practical objective of decreasing the thermal budget of a DPF and that, after a threshold concentration, there is little benefit to operating at higher doping levels. The data in Figures 20a,b were fitted to an Arrhenius expression (Eq. 1). Table 1 lists the Arrhenius parameters (frequency factors, A_{nm}'s, and activation energy, E_a) obtained.

The activation energies of Diesel particle oxidation for 25 and 100 ppm cerium-dosing rate were essentially equivalent, within experimental error, and equaled 107 and 102 kJ mol^{-1}, respectively. More interesting, perhaps, is that the activation energy of the dosed fuel was not any different from that of the undosed case (108 kJ mol^{-1}), even though the absolute oxidation rate in the range of temperature studies was some ~ 20 times faster. These results are qualitatively consistent with the study by Stanmore et al. [29]. Using the thermogravimetric method, they compared oxidation rates of cerium dosed Diesel particles with that of undosed Diesel particles at various engine conditions (idle, medium speed, and high speed). They found that the presence of the catalyst did not change the activation energy, consistent with our observation; however, their measured activation energy (210 kJ mol^{-1}) was a factor of two higher than our observation. Miyamoto et al. [32] also found an increase in the oxidation rate (Figure 13 'g') for Ca-catalyzed DPM. However, they observed a two stage oxidation process. In their TGA study, they observed an initial stage of rapid oxidation with very

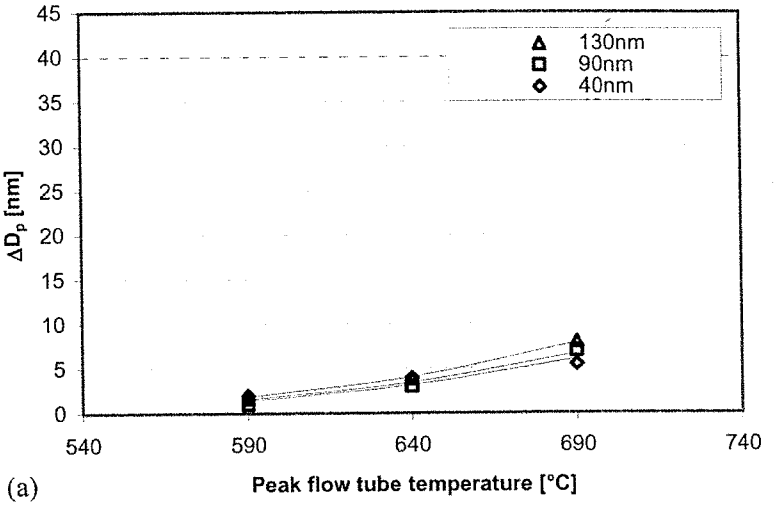

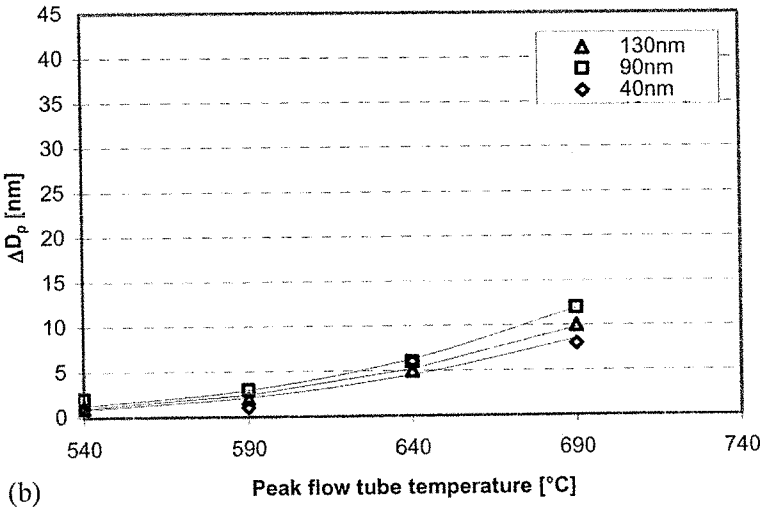

Figure 20. Particle size change as a function of peak flow tube temperature for the three initial particle sizes. (a) 25 ppm cerium dosed fuel. (b) 100 ppm cerium dosed fuel. Compare with Figure 15b for regular base fuel [37].

low activation energy (Figure 13 'h') followed by slower and higher activation energy kinetics (Figure 13 'g') of a similar magnitude to other studies. This rapid early stage is similar to an observation referred to as auto-acceleration by Lahaye et al. [43]. While our experiments are unable to resolve transients such as described above, we do note that, the general addition of metals does not seem to change the activation energy, but does increase the oxidation rate significantly.

Table 1. The preexponential factors and the activation energies of diesel soot oxidation under different loads and cerium doping for mobility diameters of 40 and 93 and 130 nm. The bio-diesel soot data is presented for 40, 89, 128 nm mobility diameter. The oxidation kinetic parameters of flame soot with and without iron doping is also shown.

	Diesel particles [37]			Bio-diesel particles [55]	Cerium-doped flame diesel particles [47]		Diffusion soot particles [56]	
	10% load	50% load	75% load		25 ppm	100 ppm	Non-iron doping	Iron doping
E_a [kJ mol^{-1}]	114	109	108	88.5	107	102	162±3	116±3
A_{40} [10^4nm K$^{-1/2}$ s^{-1}]	8.8	3.1	2.6	0.77	66	50	1200	800
A_{89} [10^4nm K$^{-1/2}$ s^{-1}]				1.5				
A_{93} [10^4nm K$^{-1/2}$ s^{-1}]	7.7	4.5	3.8		73	70	2200	1100
A_{128} [10^4nm K$^{-1/2}$ s^{-1}]				1.9				
A_{130} [10^4nm K$^{-1/2}$ s^{-1}]	11.2	5.4	4.8		86	58	3200	1800

This corroborated observation that the use of a catalyst did not reduce the activation energy. We have previously observed that Diesel soot oxidation has a lower activation energy than flame generated soot; it has been speculated that small quantities of metals from lube oil may serve as an inadvertent catalyst [37, 49]. This provides a consistent picture for the observed results, although further work is still needed to establish if, indeed, sufficient metals from lube oil are incorporated into soot. Stanmore et al. [29] observed the fall-off of the reactivity above 600 °C for cerium dosed particles, which was not seen in our work. It is possible that the, so called, auto-acceleration may be an artifact of the TGA measurements, which are notorious for being corrupted by mass and heat transfer effects as demonstrated by Mahadevan et al. [36]. From a practical point, the similarity of Ca vs. Ce might suggest the opportunity that other metals may serve the function of oxidant accelerator and that one is left with the opportunity to choose the dopant based on cost, ease of use, and environment/health concerns, as well as oxidation rate.

Literature on the health effects of a cerium additive is limited. A report [52] from the Health Effect Institute was the only extensive study, we could find on the health effect of cerium additive. The report concluded that the risk of inhaling cerium at the estimated worst-case ambient level (1.2 μg/m^3) arising from heavy Diesel traffic, using a cerium additive with a particulate trap, appears to be small. However the absence of more complete information precluded their fully assessing the possible health effects of using cerium as a fuel additive. They mentioned that risk of chronic exposure was more difficult to estimate due to the lack of adequate studies, and the possible increase in cerium emissions during the regeneration process of the particulate trap. It should be further noted that no one is proposing to use Ce or any metal as a soot suppression additive on its own. It would only be used in combination with a particle filter. Used in this manner Ce has a double benefit, it reduces the amount of soot collected in the filter, and thus the frequency of regeneration, and facilitates regeneration when it occurs.

2.5.2. *Difference between flame and diesel soot*

The flame soot and diesel soot show significantly different temperature sensitivity to oxidation (i.e. activation energy). In the previous section we saw that adding cerium oxide a known catalyst, to diesel fuel increased the oxidation rate, but did not affect the activation energy. Similarly, the addition of lubrication oil, which contains significant quantities of metal, increased the oxidation rate but did not affect the activation energy [53]. All these results point to an indirect conclusion that Diesel soots already contain metals that catalyze the oxidation of soot. The addition of metal additives to diesel may result in a decrease in soot emissions, which can be attributed to either suppressing soot inception and growth, or promoting oxidation in the combustion chamber.

The flame soot has significantly higher activation energy for oxidation than the diesel soot. It is hypothesized that metals, possibly coming from lubricating oils, within the diesel soot may be responsible for lowering the activation energy. In order to test the hypothesis metals are added to the soot in a systematic manner as described below. The TDMA method described above is used to find out the size dependent oxidation kinetics for flame soot and flame soot doped with iron.

The representative TDMA measurement for the 130 nm initial particle size with and without iron-doped soot is presented in Figure 21. For pure soot particles as shown in Figure 21a, the particle size changed by less than 1% for temperatures up to 500°C and is likely due to evaporation of volatile materials condensed on the soot particles. This fact is verified by employing nitrogen carrier gas instead of air. Above 500°C, the soot particles undergo significant oxidation and higher extents of oxidation with increasing temperature for fixed residence time. Careful observation of the profiles in Figure 21a also shows small satellite peaks. These correspond to the small fraction of particles that have two charges and are larger particles with the equivalent mobility diameter. The decrease in number density with increasing temperature can be attributed to thermophoretic deposition of soot particles to the reactor wall. The thermophoretic loss of soot particles is promoted with increasing temperature due to the higher temperature gradient. With increasing reactor temperature a greater fraction of the aerosol is lost to the walls at the exit of the reactor. However, since thermophoretic velocity is particle size independent we expect no changes to the resulting size distribution. Since our analysis relies on size change, and does not depend on number concentration, these losses have no impact on our data analysis. Figure 21b shows the evolution of size distribution of iron-doped soot nanoparticles at various oxidation temperatures. Unlike the pure soot particles, the mean size of the iron-doped soot particles decreased significantly even at 500°C. At the higher temperature range (700°C-900°C), particle shrinkage ceases as shown in the inserted graph. Here we believe we have completely burned out the soot leaving behind iron which also has presumably been oxidized. If we assume that the iron nanoparticles are oxidized to Fe_2O_3, and using the bulk densities of iron and iron oxide with 7.86 and 5.18 g/cc, respectively, we can work backwards to determine the effective size of the original iron constituent. In this way the 60 nm peak corresponds to a volume equivalent diameter of 41 nm for pure iron. Working back further we can determine that the relative volume loading from the original 131 nm soot particle we started at, gives a ~ 3% iron volume loading relative to soot mass.

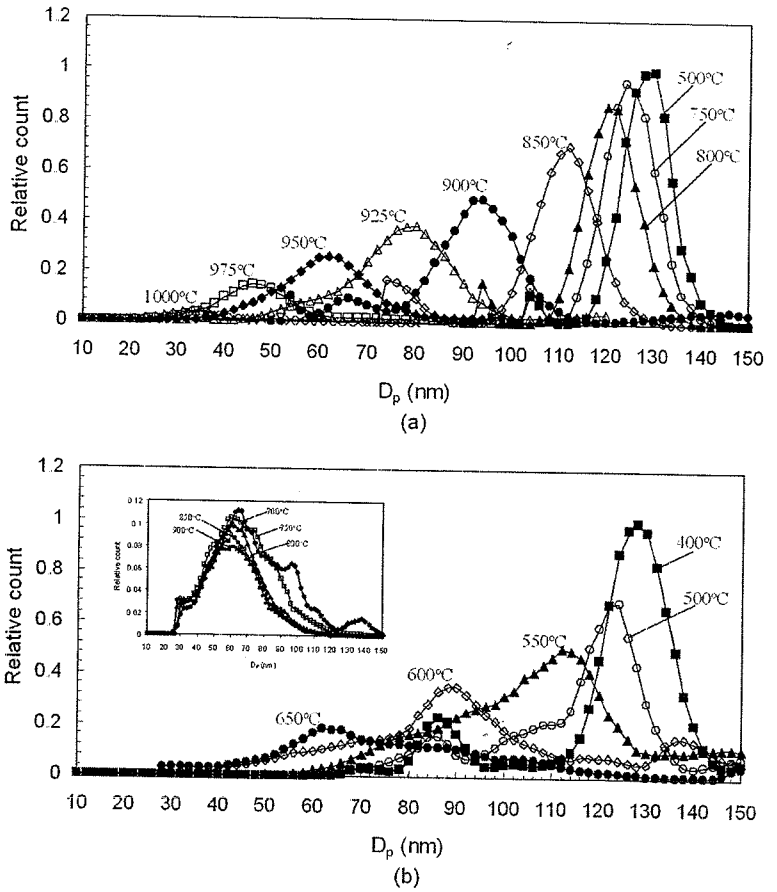

Figure 21. TDMA results for soot oxidation in air for various temperatures from 400 to 1000°C: (a) non iron-doped soot nanoparticles and (b) iron-doped soot nanoparticles. Initial mobility diameter = 130 nm.

Figure 22 presents the size decrease measured by TDMA system (symbols) and the fitted into Eqs. 1-6. The open circle data represent the iron-doped case clearly show a much reduced on-set temperature relative to the undoped case (solid symbols). Table 1 summarizes the kinetic parameters, (A_{40}, A_{93}, A_{130}, and E_a) found by a best fit to the experimental data, which are also plotted in Figure 22 as the solid lines. We first note a significant decrease in the activation energy from 162±3 kJ/mol for the pure soot, to 116±3 kJ/mol for the iron-doped case. The pre-exponential factors for the iron-doped soot particles are slightly smaller (factor of 2) as compared to the undoped case. However, due to the sensitivity of the fit to the activation energy it is difficult to assess if this is a real effect or simply an artifact of the fit. The absolute values of the A factor are consistent with the data shown in earlier sections. The slight size dependent rates observed, whereby the larger particles have an increased apparent oxidation rate

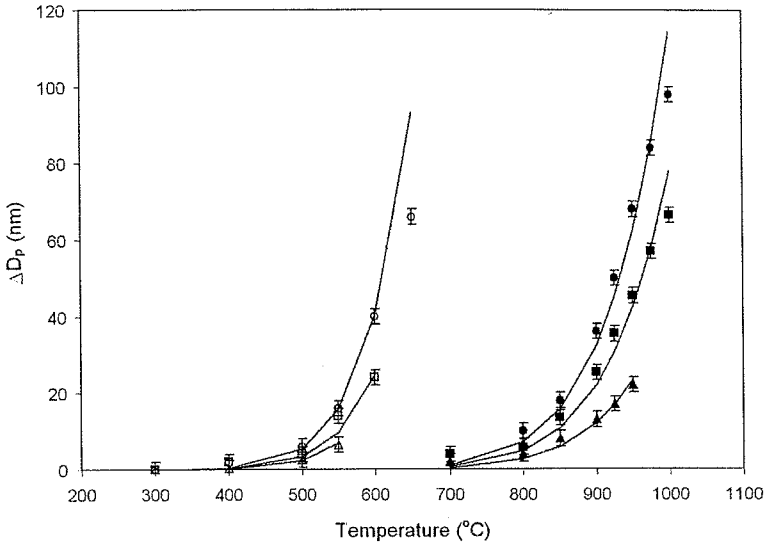

Figure 22. Comparison of particle size change as a function of temperature for the 40 nm (triangles), 93 nm (squares) and 130 nm (circles) initial sizes of non iron-doped (solid symbols) and iron-doped (open symbols) soot nanoparticles. Solid lines are the fitted models based upon the kinetic parameters of Arrhenius equation as shown in Table 1.

has been discussed in our prior work and have been attributed to an assumption made of constant effective density. One also notes that there is a large difference in pre-exponential factors between diesel and flame soot particles. This observation, as seen above, is presumably related to some inherent chemical difference between flame and diesel generated soot which has not yet to be addressed adequately. For example hydrogen content is generally higher and diesel soot also generally contains a significant amount of sulfur and nitrogen [34].

Since the volume fraction of metal content in the current flame soot matrix (~3% volume fraction) is larger than that of diesel soot (~1% volume fraction), we reduced the iron addition down by a factor of 5 (~0.02 mol % of the fuel) to observe the effect of the amount of iron loading on the activation energy and A factor. For comparison, 93 nm initial iron-doped flame soot particles were selected for TDMA measurement. The kinetic parameters found were 161±3 kJ mol^{-1} [2.2 10^7 nm $K^{-1/2}$ s^{-1}], 133±3 kJ mol^{-1} [1.2 10^7 nm $K^{-1/2}$ s^{-1}], and 116±3 kJ mol^{-1} [1.1 10^7 nm $K^{-1/2}$ s^{-1}] for non-iron loading, 0.02 mol % iron loading, and 0.1 mol % iron loading cases, respectively. These results are consistent with the hypothesis that small quantities of metal seeding in soot matrix increases the reactivity of the resulting soot nanoparticles by significantly decreasing their activation energy. These results are consistent with the idea that small quantities of metals during diesel combustion may play an important role in soot abatement.

2.6. Conclusions

In this paper we summarize our studies on the oxidation kinetics of size selected soot particles. The size dependent Arrhenious kinetic parameters are measured using two methods: (a) direct observation by TEM and (b) TDMA method. We found that the oxidation rate of flame soot measured by the TEM method at low temperatures (< 800 K) was higher than that measured by TDMA method over the temperature range 800°-1120° C. Using the TDMA method, the activation energy of soot oxidation in air was equal to 163 kJ mol^{-1}.

The TDMA method is also used to measure oxidation kinetics for diesel and bio-diesel soot. The activation energy of diesel soot (114 kJ/mol) is found to be higher than the bio-diesel soot (88.5 kJ/mol). The faster oxidation kinetics of bio-diesel fuel should facilitate regeneration when used with a diesel particulate filter.

A comparison of the behavior of flame vs. Diesel soot suggest that Diesel soot behaves as though it has small amounts of catalytically active metals, which we confirm by adding metal to flame soot. These results are consistent with idea that metals in lubrication oils are incorporated into soot formed during combustion. More importantly perhaps is that combustion modeling of soot formation in Diesel should incorporate the understanding that metals will play a role not only in soot oxidation but soot production as well, and that nascent flame soot studies may not capture this effect.

Nomenclature

A	Pre-exponential factor
A_{nm}	Frequency factor for each initial soot particle size
d_a	Projected area equivalent diameter
d_m	Mobility diameter
E_a	Activation energy
m_i	Mass of soot particle
R	Universal gas constant
T	Temperature
T	Time
u_m	Mean flow velocity
$\dot{w}$	Mass based surface specific rate
X	Horizontal position in the tube
X	Length of the tube
$\rho_{effective}$	Effective density of soot particle
ρ_s	Mass density of soot particle
τ_o	Characteristic residence time

REFERENCES

1. A. Chung, A. A. Lall, S. E. Paulson, Atmos. Environ. (2007) in review.
2. T. L. Barone, A. A. Lall, Y. F. Zhu, R. C. Yu, S. K. Friedlander, J. Nanopart. Res. 8(5) (2006) 669-680.
3. C. Venkataraman, G. Habib, A. Eiguren-Fernandez, A. H. Miguel, S. K. Friedlander, Science 307(5714) (2005) 1454-1456.
4. T. C. Bond, Geophys. Res. Lett. 28(21) (2001) 4075-4078.
5. R. J. Santoro, H. G. Semerjian, R. A. Dobbins, Combust. Flame 51(2) (1983) 203-218.
6. M. S. Graboski, R. L. McCormick, Prog. Energy Combust. Sci. 24(2) (1998) 125-164.
7. A. K. Babu, G. Devaradjane, SAE Technical Paper Series (2003) 2003-2001-0767.
8. P. H. Abelson, Science 1995(268) (1995) 955.
9. O. Schröder, J. Krahl, A. Munack, J. Bünger, SAE Technical Paper Series (1999) 1999-1901-3561.
10. A. Monyem, J. H. Van Gerpen, Biomass Bioenergy 20(2001) 317-325.
11. J. Krahl, A. Munack, O. Schröder, H. Stein, J. Bünger, SAE Technical Paper Series (2003) 2003-2001-3199.
12. G. L. Finch, C. H. Hobbs, L. F. Blair, E. B. Barr, F. F. Hahn, R. J. Jaramillo, J. E. Kubatko, T. H. March, R. K. White, J. R. Krone, M. G. Ménache, K. J. Nikula, J. L. Mauderly, J. Van Gerpen, M. D. Merceica, B. Zielinska, L. Stankowski, K. Burling, S. Howell, Inhalation Toxicology 14 (2002) 1017-1048.
13. J. B. Williams, Eur. J. Lipid Sci. Technol. 104(6) (2002) 361-362.
14. W. Korbitz, Renewable Energy 16(1-4) (1999) 1078-1083.
15. R. L. Pereira, W. H. Maria, Appl. Biochem. Biotechnol.121 (2005) 807.
16. http://www.soyatech.com/bluebook/news/viewarticle.ldml?a=20041214-20041216.
17. H. J. Jung, D. B. Kittelson, M. R. Zachariah, Combust. Flame 136(4) (2004) 445-456.
18. P. Meakin, B. Donn, G. W. Mulholland, Langmuir 5 (1989) 510.
19. S. N. Rogak, U. Baltensperger, R. C. Flagan, Aerosol Sci. Technol. 14 (1991) 447.
20. A. Schmidt-Ott, U. Baltensperger, H. W. Gäggeler, D. T. Jost, J. Aerosol Sci. 21 (1990) 711.
21. S. H. Kim, K. S. Woo, B. Y. H. Liu, M. R. Zachariah, J. Colloid Interface Sci. 282(1) (2005) 46-57.
22. K. J. Higgins, H. J. Jung, D. B. Kittelson, J. T. Roberts, M. R. Zachariah, J. Phys. Chem. A 106(1) (2002) 96-103.
23. T. Tanaka, in 22nd International Vienna Engine Symposium, Vol. 2, OVK and Technical University of Vienna, 2001.
24. F. A. Heckman, Rubber Chem. Technol. 37 (1964) 1245.
25. P. Gilot, F. Marcuccilli, G. Prado, Corrosion of Advanced Ceramics (1963) 329-339.
26. W. Hess, M. C. R. Herd, in Carbon Black, J.-B. Donnet, R. C. Bansal, M.-J. Wang (Eds.) Marcel Dekker, NY, 1993, 2nd ed.
27. I. M. Kennedy, Prog. Energy Combust. Sci. 23 (1997) 95.
28. J. Nagle, R. F. Strickland-Constable, in Fifth Carbon Conference, Vol. 1, Pergamon, Oxford, 1962, pp. 154-164.
29. B. Stanmore, B. J.-F., P. Gilot, SAE Technical Paper Series (1999) 1999-1901-0115.
30. K. J. Higgins, H. J. Jung, D. B. Kittelson, J. T. Roberts, M. R. Zachariah, Environ. Sci. Technol. 37(9) (2003) 1949-1954.
31. J. v. Doorn, J. Varloud, P. Mériaudeau, V. Perrichoni, Appl. Catal., B 1 (1992) 117.
32. N. Miyamoto, H. Zhixin, O. Hideyuki, SAE Technical Paper Series (1988) 881224.
33. K. Otto, M. H. Sieg, M. Zinbo, L. Bartosiewicz, SAE Technical Paper Series (1980) 800336.
34. A. F. Ahlström, C. U. I. Odenbrand, Carbon 3 (1989) 475.

35. T. Ishiguro, N. Suzuki, Y. Fujitani, H. Morimoto, Combust. Flame 85 (1991) 1.
36. R. Mahadevan, D. Lee, H. Sakurai, M. R. Zachariah, J. Phys. Chem. A 106(46) (2002) 11083-11092.
37. K. J. Higgins, H. Jung, D. B. Kittelson, J. T. Roberts, M. R. Zachariah, Environ. Sci. Technol. 37 (2003) 1949-1954.
38. K. J. Higgins, H. Jung, D. B. Kittelson, J. T. Roberts, M. R. Zachariah, J. Phys. Chem. A 106 (2002) 96-103.
39. K. Park, C. Feng, D. B. Kittelson, P. H. McMurry, Environ. Sci. Technol. 37 (2003) 577-583.
40. N. Miyamoto, H. Zhixin, A. Harada, H. Ogawa, T. Murayama, SAE Technical Paper Series (1987) 871612.
41. J. M. Valentine, J. D. Peter-Hoblyn, G. K. Acres, SAE Technical Paper Series (2000) 2000-2001-1934.
42. G. Skillas, Z. Qian, U. Baltensperger, U. Matter, H. Burtscher, Combust. Sci. Technol. 154 (2000) 259-273.
43. J. Lahaye, S. Boehm, P. H. Chambrion, P. Ehrburger, Combust. Flame 104 (1996) 199-207.
44. M. Kasper, K. Sattler, K. Siegmann, U. Matter, H. C. Siegmann, J. Aerosol Sci. 30 (1999) 217.
45. N. Kyriakis, Z. Samaras, E. Vouitsis, T. Manikas, T. Seguelong, G. Blanchard, SAE Technical Paper Series (2002) 2002-2001-0429.
46. K. Pattas, N. Kyriakis, Z. Samaras, T. Manikas, A. Mihailidis, W. Mustel, P. Rouveirolles, SAE Technical Paper Series (1998) 980543.
47. H. J. Jung, D. B. Kittelson, M. R. Zachariah, Combust. Flame 142(3) (2005) 276-288.
48. H. Sakurai, H. J. Tobias, K. Park, D. Zarling, S. Docherty, D. B. Kittelson, P. H. McMurry, P. J. Ziemann, Atmos. Environ. 37(9-10) (2003) 1199-1210.
49. K. J. Higgins, H. Jung, D. B. Kittelson, J. T. Roberts, M. R. Zachariah, J. Phys. Chem. 106 (2002) 96-103.
50. H. Jung, D. B. Kittelson, M. R. Zachariah, Combust Flame (2003) submitted.
51. S. V. Hering, S. K. Friedlander, J. J. Collins, L. W. Richards, Environ. Sci. Technol. 13 (1979) 184-188.
52. M. G. Costantini, R. Henderson, D. S. Greenbaum, H. Greim, E. D. Pellizzari, R. Sawyer, J. Warren, J. Ball, S. Cadle, J. M. Davis, N. Englert, D. B. Kittelson, A. Mayer, J. McAughey, R. McClellan, R. F. Phalen, G. Simon, M. Waalkes, Health Effects Institute (2001) Communication 9.
53. H. Jung, D. B. Kittelson, M. R. Zachariah, SAE Paper 2003-01-3179 (2003).
54. A. A. Lall, S. K. Friedlander, J. Aerosol Sci. 37(3) (2006) 260-271.
55. H. J. Jung, D. B. Kittelson, M. R. Zachariah, Environ. Sci. Technol. 40(16) (2006) 4949-4955.
56. S. H. Kim, R. A. Fletcher, M. R. Zachariah, Environ. Sci. Technol. 39(11) (2005) 4021-4026.